

Optimal Multivariable Control for Wide Output Regulation and Full-Range Efficiency Optimization in LCC-LCC Compensated Wireless Power Transfer Systems

Zhu, Gangwei; Dong, Jianning; Yu, Guangyao; Shi, Wenli; Riekerk, Calvin; Bauer, Pavol

DOI

[10.1109/TPEL.2024.3414157](https://doi.org/10.1109/TPEL.2024.3414157)

Publication date

2024

Document Version

Final published version

Published in

IEEE Transactions on Power Electronics

Citation (APA)

Zhu, G., Dong, J., Yu, G., Shi, W., Riekerk, C., & Bauer, P. (2024). Optimal Multivariable Control for Wide Output Regulation and Full-Range Efficiency Optimization in LCC-LCC Compensated Wireless Power Transfer Systems. *IEEE Transactions on Power Electronics*, 39(9), 11834-11848. <https://doi.org/10.1109/TPEL.2024.3414157>

Important note

To cite this publication, please use the final published version (if applicable). Please check the document version above.

Copyright

Other than for strictly personal use, it is not permitted to download, forward or distribute the text or part of it, without the consent of the author(s) and/or copyright holder(s), unless the work is under an open content license such as Creative Commons.

Takedown policy

Please contact us and provide details if you believe this document breaches copyrights. We will remove access to the work immediately and investigate your claim.

Green Open Access added to TU Delft Institutional Repository

'You share, we take care!' - Taverne project

<https://www.openaccess.nl/en/you-share-we-take-care>

Otherwise as indicated in the copyright section: the publisher is the copyright holder of this work and the author uses the Dutch legislation to make this work public.

Optimal Multivariable Control for Wide Output Regulation and Full-Range Efficiency Optimization in *LCC–LCC* Compensated Wireless Power Transfer Systems

Gangwei Zhu ¹, Student Member, IEEE, Jianning Dong ², Senior Member, IEEE,
Guangyao Yu ³, Student Member, IEEE, Wenli Shi ⁴, Student Member, IEEE,
Calvin Riekerk ⁵, Student Member, IEEE, and Pavol Bauer ⁶, Senior Member, IEEE

Abstract—This article presents an optimal multivariable control (OMC) strategy for the *LCC–LCC* compensated wireless power transfer systems. To mitigate reactive power and achieve higher efficiency, the proposed OMC method incorporates dual-side hybrid modulation and primary-side switch-controlled-capacitor (SCC) tuning into the triple-phase-shift (TPS) control. First, the impact of hybrid modulation and SCC tuning on the system characteristics is investigated. The inverter and rectifier zero-voltage-switching (ZVS) conditions are then analyzed to achieve dual-side ZVS with minimal reactive power. Furthermore, a multivariable optimization problem is established based on the power loss analysis. The solution to this problem provides optimal control variables that minimize the overall system loss. Through collaborative modulation and control of the inverter, rectifier, and SCC, the proposed method reduces the rms values of the currents and lowers the turn-off currents for the converters. As a result, this approach improves efficiency in both light- and heavy-load conditions, enabling wide output regulation and full-range efficiency optimization simultaneously. Finally, the proposed method is benchmarked with the existing TPS method. Experimental results demonstrate that the proposed method achieves higher dc-to-dc efficiency in the power range of 0.2–2.2 kW, with a maximum efficiency improvement of up to 6.3%.

Index Terms—Hybrid modulation, multivariable control, switch-controlled-capacitor (SCC), wireless power transfer (WPT).

I. INTRODUCTION

THROUGH enabling safe, flexible, and automated charging without the necessity for physical cables, wireless power

Manuscript received 9 January 2024; revised 26 March 2024 and 7 May 2024; accepted 7 June 2024. Date of publication 13 June 2024; date of current version 16 July 2024. This work was supported by China Scholarship Council (CSC) under Grant 202106230112. The work of Gangwei Zhu was supported by the CSC at the Delft University of Technology, the Netherlands. Recommended for publication by Associate Editor S. A. Khajehoddin. (Corresponding author: Jianning Dong.)

The authors are with the DC System, Energy Conversion and Storage Group, Faculty of Electrical Engineering, Mathematics and Computer Science, Delft University of Technology, 2624 Delft, The Netherlands (e-mail: g.zhu-2@tudelft.nl; j.dong-4@tudelft.nl; g.yu-1@tudelft.nl; w.shi-3@tudelft.nl; c.rieker@tudelft.nl; p.bauer@tudelft.nl).

Color versions of one or more figures in this article are available at <https://doi.org/10.1109/TPEL.2024.3414157>.

Digital Object Identifier 10.1109/TPEL.2024.3414157

transfer (WPT) technology holds great potential in many industrial applications, such as consumer electronics [1], medical devices [2], marine facilities [3], and electric vehicles (EVs) [4]. In these applications, batteries commonly serve as the loads of the system. To address significant battery load variations during the charging process, achieving wide output power regulation is indispensable. Moreover, improving transmission efficiency is regarded as another important objective to facilitate efficient wireless battery charging.

In recent years, extensive approaches have been investigated to achieve wide power regulation while improving efficiency for WPT systems. These methods can be roughly classified into the following three groups:

- 1) dc voltage regulation;
- 2) inverter/rectifier modulation;
- 3) frequency tuning.

One commonly adopted approach for achieving wide power regulation involves adjusting the dc input and output voltages. Typically, this is accomplished by incorporating dc-dc converters at the front and/or back end of the system [5], [6], [7]. Regulating dc voltages allows for a wide range of adjustments to the delivered power. However, the introduction of additional dc-dc converters results in increased power losses, higher costs, and a reduction in power density.

To eliminate the need for dc-dc converters, phase-shift modulation is frequently employed within the inverter and/or rectifier to enable wide output tuning in WPT systems. In addition to applying phase-shift modulation to the primary-side inverter [8], the secondary-side rectifier can also be actively modulated by replacing the passive diode rectifier with an active rectifier [9]. Implementing dual-side phase shift modulation on both the inverter and rectifier significantly extends the operating range of the system. However, the dual-phase-shift (DPS) method encounters substantial efficiency degradation due to hard switching of power switches [10]. Based on the DPS method, a triple-phase-shift (TPS) modulation strategy was further proposed to enable wide-range zero-voltage-switching (ZVS) [11]. In the TPS method, the phase difference between the inverter and rectifier ac voltages is dynamically adjusted to achieve

ZVS under load variations. Nonetheless, this approach leads to a significant increase in reactive power under light-load conditions. Moreover, as the dc output voltage of the system varies, the TPS method introduces additional reactive power, leading to a notable reduction in transmission efficiency. Aside from phase-shift modulation, other modulation techniques, such as pulse density modulation (PDM) [12] and ON-OFF keying (OOK) modulation [13], have been introduced to enable ZVS. By maintaining a constant pulsewidth for the output voltage, these modulations offer a broad ZVS capability while reducing reactive power. However, the PDM methods lead to noticeable current distortions and output voltage ripple due to the irregular pulse distributions, whereas the OOK techniques result in significant surge currents and output voltage ripple due to the “OFF” state.

In combination with dc voltage regulation or phase shift modulation, frequency tuning is also applied to achieve wide power tuning. Mostafa et al. [14] proposed a hybrid voltage and frequency tuning method to allow for wide power regulation in wireless EV charging. In addition, a variable frequency-based phase shift modulation was proposed in [15] to implement wide ZVS for the inverter. However, it is noteworthy that tuning frequency is susceptible to the bifurcation phenomenon [16], [17]. Consequently, existing frequency tuning strategies necessitate careful design of system parameters to prevent the occurrence of bifurcation.

Within the above approaches, the TPS method was widely investigated as it enables wide-range ZVS and power regulation while eliminating extra dc–dc converters, mitigating significant output voltage ripple, and preventing frequency bifurcation. To improve efficiency under light-load conditions, hybrid modulation strategies were proposed for the SS compensation topology in [18] and [19], where the half-bridge (HB) mode was introduced for delivering power at light loads. However, these approaches are not able to effectively improve efficiency as the output power approaches the full level. In addition, Fu et al. [20] integrated a secondary-side switch-controlled-capacitor (SCC) into the *LCC-LCC* topology to reduce the reactive power at wide output voltages. Nevertheless, a notable efficiency drop was observed in this method when dealing with light-load conditions. Existing methods lack effective strategies for simultaneously improving efficiency under both light- and heavy-load conditions.

To fill up the above research gaps, this article proposes an optimal multivariable control (OMC) strategy based on the *LCC-LCC* compensation network. The *LCC-LCC* topology is investigated as it maintains constant coil currents despite coupling changes while providing greater design flexibility. Moreover, the main contributions of this article are summarized as follows.

- 1) A multivariable control method featuring six control variables is proposed. By introducing dual-side hybrid modulation and a primary-side SCC, the proposed method achieves significantly reduced reactive power when compared with the existing TPS method.
- 2) ZVS conditions under hybrid modulation and SCC tuning are investigated for the asymmetric *LCC-LCC* topology,

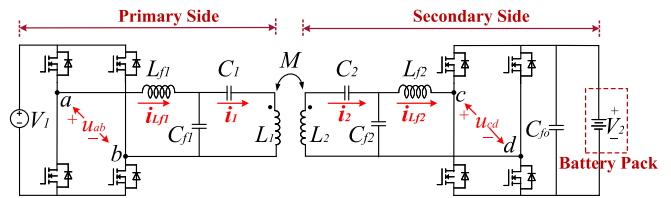


Fig. 1. Topology of the *LCC-LCC* compensated WPT system.

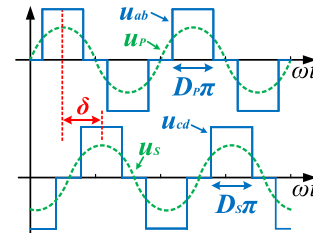


Fig. 2. Typical operating waveforms of the existing TPS modulation.

and the corresponding control variables are derived to implement dual-side optimal ZVS.

- 3) A multivariable optimization problem is formulated based on the power loss analysis. By solving this problem, optimal control variables are obtained to minimize the overall loss of the system.
- 4) Through cooperative modulation and control of the inverter, rectifier, and SCC, wide output power regulation is achieved without introducing extra dc–dc converters. More importantly, the proposed method improves efficiency in both light- and heavy-load conditions, thus enabling full-range efficiency optimization for the system.

The rest of this article is organized as follows. Section II presents the fundamental characteristics of the *LCC-LCC* topology and demonstrates the limitations of the existing TPS method. Subsequently, Section III elaborates on the design principles and control framework of the proposed OMC method. Experimental results are further presented in Section IV. Finally, Section V concludes this article.

II. PROBLEM FORMULATION

A. System Configurations

Fig. 1 presents the topology of the *LCC-LCC* compensated WPT system, where an active rectifier is adopted on the secondary side to replace the passive diode rectifier. The dc input voltage is represented by V_1 , while the battery voltage is denoted by V_2 . Moreover, the mutual inductance of the contactless coupler is expressed as $M = k\sqrt{L_1L_2}$, where k is the coupling coefficient, and L_1 and L_2 are the primary and secondary self-inductances, respectively. To compensate the leakage inductances of the loose coupler, parameters of the *LCC-LCC* topology are designed as $\omega_n L_{f1} = 1/(\omega_n C_{f1})$, $\omega_n L_{f1} = \omega_n L_1 - 1/(\omega_n C_1)$, $\omega_n L_{f2} = 1/(\omega_n C_{f2})$, and $\omega_n L_{f2} = \omega_n L_2 - 1/(\omega_n C_2)$, where ω_n is the resonant frequency [21].

Fig. 2 demonstrates the typical operating waveforms of the existing TPS modulation. Here, u_{ab} and u_{cd} are the inverter

output voltage and rectifier input voltage, respectively; u_P and u_S are the fundamental component of u_{ab} and u_{cd} , respectively; D_P and D_S are the duty cycles of u_{ab} and u_{cd} , respectively; δ is the phase difference between u_{ab} and u_{cd} . According to the fundamental harmonic analysis (FHA) method, the phasor forms of u_P and u_S , denoted as \dot{U}_P and \dot{U}_S , are given as

$$\dot{U}_P = \frac{2\sqrt{2}}{\pi} V_1 \sin\left(\frac{D_P\pi}{2}\right) \angle 0, \dot{U}_S = \frac{2\sqrt{2}}{\pi} V_2 \sin\left(\frac{D_S\pi}{2}\right) \angle -\delta. \quad (1)$$

According to [11], when applying the TPS modulation into the symmetrical *LCC-LCC* topology, the maximum efficiency tracking of the resonant tank can be achieved when

$$\frac{\sin(D_S\pi/2)}{\sin(D_P\pi/2)} = \frac{V_1}{V_2}. \quad (2)$$

Moreover, based on the work in [11], both the inverter and rectifier ZVS are achieved by tuning the phase difference angle δ in the TPS method. The value of δ can be expressed as $\delta = \pi/2 + \Delta\delta$, where $\Delta\delta$ is the compensation phase angle. As $\Delta\delta$ increases, the deviation between δ and $\pi/2$ increases as well, resulting in a larger reactive power in the resonant tank while facilitating ZVS. Specifically, to realize the inverter ZVS with minimal reactive power, $\Delta\delta$ should be designed as

$$\Delta\delta_1 = \cos^{-1} \left[\frac{-2\pi X I_{ZVS} + V_1(D_P\pi^2 - 8\sin^2(D_P\pi/2))}{8\alpha k V_2 \sin(D_S\pi/2)} \right] - D_P\pi/2 \quad (3)$$

where I_{ZVS} is the threshold ZVS current to charge/discharge the equivalent output capacitance C_{oss} of the power switches within the dead time; $\alpha = L_1/L_{f1} = L_2/L_{f2}$; and $X = \omega L_1 = \omega L_2$. Similarly, the rectifier ZVS with minimal reactive power can be achieved by designing $\Delta\delta$ as

$$\Delta\delta_2 = \cos^{-1} \left[\frac{-2\pi X I_{ZVS} + V_2(D_S\pi^2 - 8\sin^2(D_S\pi/2))}{8\alpha k V_1 \sin(D_P\pi/2)} \right] - D_S\pi/2. \quad (4)$$

Consequently, to implement ZVS for both the inverter and rectifier in the TPS method, $\Delta\delta$ is configured as

$$\Delta\delta = \max(\Delta\delta_1, \Delta\delta_2). \quad (5)$$

B. Limitations of Existing TPS Method

Although the existing TPS method is able to achieve maximum efficiency tracking and wide ZVS, it does encounter significant limitations when dealing with nonunity dc voltage gain and asymmetric *LCC-LCC* networks. The specific limitations of the existing TPS method are elaborated as follows.

Considering the voltage specifications of the system input and output, it is common practice for the WPT systems to be designed for nonunity dc voltage gain. In addition, the asymmetric coil structure is also frequently employed to enhance the coil misalignment tolerance [22], as well as to optimize the component parameters and stresses [23]. Therefore, it is preferable to further extend the existing analysis to the asymmetric *LCC-LCC* networks. In this article, both the nonunity dc voltage gain and

TABLE I
PARAMETERS OF THE INVESTIGATED WPT SYSTEM

Symbol	Parameters	Value	Unit
M	Mutual inductance	94.6	μH
L_1	Primary coil inductance	335.6	μH
L_2	Secondary coil inductance	224.2	μH
C_1	Primary series capacitance	14.8	$n\text{F}$
C_2	Secondary series capacitance	25.3	$n\text{F}$
C_{f1}	Primary parallel capacitance	33.1	$n\text{F}$
C_{f2}	Secondary parallel capacitance	41.3	$n\text{F}$
L_{f1}	Primary compensation inductance	103.8	μH
L_{f2}	Secondary compensation inductance	83.8	μH
R_1	Primary coil resistance	0.45	Ω
R_2	Secondary coil resistance	0.30	Ω
R_{Lf1}	Primary inductor resistance	0.20	Ω
R_{Lf2}	Secondary inductor resistance	0.14	Ω
f_s	Resonant switching frequency	85	kHz
V_1	DC input voltage	300	V
V_2	DC output voltage	500	V

the asymmetric network design are considered. The detailed parameters of the investigated WPT system are demonstrated in Table I.

When the asymmetric coil structure is considered, a more general mathematical analysis is essential. Based on the FHA method and applying Kirchoff's voltage law (KVL), optimal ZVS criteria shown in (3) and (4) are rederived as

$$\Delta\delta_1 = \cos^{-1} \left\{ \frac{1}{8MV_2 \sin(D_S\pi/2)} \times [-2\pi\omega L_{f1}L_{f2}I_{ZVS} + V_1L_{f2}(D_P\pi^2 - 8\sin^2(D_P\pi/2))] \right\} - D_P\pi/2 \quad (6)$$

$$\Delta\delta_2 = \cos^{-1} \left\{ \frac{1}{8MV_1 \sin(D_P\pi/2)} \times [-2\pi\omega L_{f1}L_{f2}I_{ZVS} + V_2L_{f1}(D_S\pi^2 - 8\sin^2(D_S\pi/2))] \right\} - D_S\pi/2. \quad (7)$$

Besides, the efficiency of the resonant tank is rederived as

$$\eta \approx \omega M L_{f1} L_{f2} |\sin(\delta)| \times [(R_2 L_{f1}^2 + M^2 R_{Lf1}) T_{ac} + (R_1 L_{f2}^2 + M^2 R_{Lf2}) / T_{ac} + \omega M L_{f1} L_{f2} |\sin(\delta)|]^{-1} \quad (8)$$

where $T_{ac} = |\dot{U}_S|/|\dot{U}_P|$ indicates the ac voltage gain of the resonant tank. Here, the derivation of (8) follows the analysis in [11] and extends it to the asymmetric networks. According to [11], assumptions are made as follows.

- 1) The converter losses are neglected.
- 2) The power losses of the resonant circuits are modeled with R_1 , R_2 , R_{Lf1} , and R_{Lf2} , where R_1 and R_2 are the equivalent loss resistances of coil branches, while R_{Lf1} and R_{Lf2} are the equivalent loss resistances of inductor branches.
- 3) The power losses caused by harmonics are neglected, and the FHA method is adopted for loss analysis.

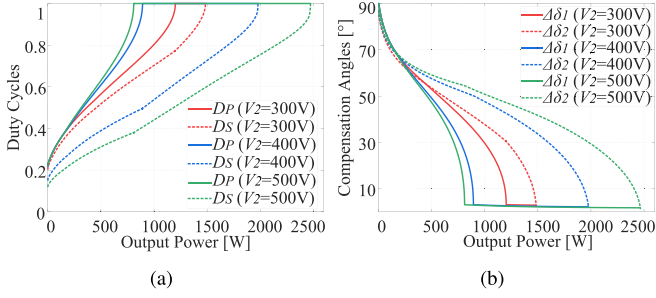


Fig. 3. Variations of (a) the duty cycles D_P and D_S and (b) the compensation angle $\Delta\delta$ under various output voltages and power levels.

As evident from (8), the maximum efficiency of the resonant tank is achieved when T_{ac} satisfy

$$T_{ac_opt} = \sqrt{\frac{bR_1 + cR_{Lf2}}{R_2/b + cR_{Lf1}}} \quad (9)$$

where $b = L_{f2}/L_{f1}$ and $c = M^2/(L_{f1}L_{f2})$. Further, substituting (1) into (9) yields

$$\frac{\sin(D_S\pi/2)}{\sin(D_P\pi/2)} = \frac{V_1}{V_2} \sqrt{\frac{bR_1 + cR_{Lf2}}{R_2/b + cR_{Lf1}}} \quad (10)$$

Due to the asymmetric parameters between the primary and secondary sides, as shown in (9), the maximum efficiency of the resonant tank is no longer achieved when $T_{ac} = 1$. Conversely, in the presence of nonunity dc voltage gain and asymmetric network design, the duty cycles D_P and D_S need to be adjusted in an inconsistent manner to realize maximum efficiency tracking, as illustrated in (10). To visualize this point of view, the values of D_P and D_S as functions of the output power are depicted in Fig. 3(a). As shown in Fig. 3(a), there is a considerable disparity between the values of D_P and D_S as the output power varies. Moreover, the asymmetric parameters also result in a distinct difference in the compensation angles $\Delta\delta_1$ and $\Delta\delta_2$, as illustrated in Fig. 3(b).

Observing Fig. 3 indicates that the existing TPS method exhibits the following two limitations.

- 1) As the output power decreases, the duty cycles D_P and D_S are reduced accordingly. Consequently, a significantly increased compensation angle $\Delta\delta$ is required for ZVS, leading to considerable reactive power under light-load conditions.
- 2) The compensation angle $\Delta\delta$ is selected as the maximum value of $\Delta\delta_1$ and $\Delta\delta_2$ to guarantee ZVS for both the inverter and rectifier. However, in the cases of asymmetric parameters, significant disparity is observed in $\Delta\delta_1$ and $\Delta\delta_2$. Notably, as the output voltage deviates from the unity value, this difference becomes more pronounced. The substantial gap between $\Delta\delta_1$ and $\Delta\delta_2$ makes it unfeasible to achieve dual-side ZVS with minimal reactive power on both the primary and secondary sides. For instance, considering the scenario of $V_2 = 500$ V, as depicted by the green curves in Fig. 3(b), although the inverter ZVS can be achieved with $\Delta\delta_1$, $\Delta\delta$ has to be selected as $\Delta\delta_2$

TABLE II
CONTROL OBJECTIVES OF THE PROPOSED OMC METHOD

Variable	Description	Control Objective
D_P	Inverter duty cycle	Maximum efficiency tracking
D_S	Rectifier duty cycle	Wide power regulation
$\Delta\delta$	Compensation phase angle	ZVS for the rectifier
θ	SCC conduction angle	ZVS for the inverter
K_P	Inverter operating mode	Reducing reactive power
K_S	Rectifier operating mode	Under light-load conditions

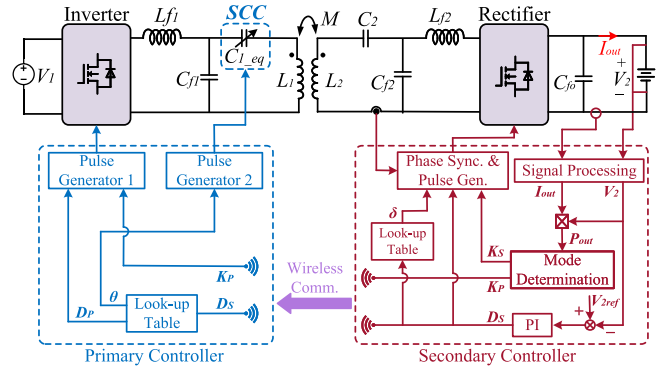


Fig. 4. Control block diagram of the proposed OMC method.

($\Delta\delta_2$ is significantly larger than $\Delta\delta_1$ in most power ranges when $V_2 = 500$ V) to ensure the rectifier ZVS, leading to a substantial excess of reactive power on the primary side.

III. PROPOSED OMC

In this article, the abovementioned challenges are addressed from two perspectives. First, the hybrid modes of the converters, including the full-bridge (FB) and HB modes, are considered to reduce the reactive power under light-load conditions. Here, the inverter operating mode is denoted as K_P , while the rectifier mode is indicated by K_S . Second, a primary-side SCC is introduced to facilitate the ZVS control, thus minimizing reactive power on both the primary and secondary sides. The SCC conduction angle is denoted as θ . The introduction of K_P , K_S , and θ into the TPS method forms a multivariable control featuring six degrees of freedom. The objectives of each control variable are demonstrated in Table II, while implementation details of the proposed method are elaborated in the following section.

A. Control Block Diagram

Fig. 4 presents the control block diagram of the proposed OMC approach. As illustrated in Fig. 4, the dc output voltage V_2 and current I_{out} are first measured. After the signal processing circuits, V_2 and I_{out} are multiplied to obtain the output power P_{out} . Based on the measured P_{out} , the inverter and rectifier modes K_P and K_S are selected through the mode determination module. Moreover, a proportional-integral (PI) controller is employed to regulate the rectifier duty cycle D_S for voltage tracking. According to the proposed optimization approach, as

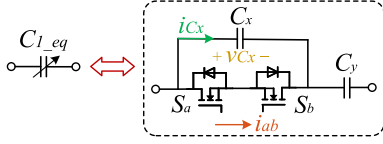


Fig. 5. Topology of the adopted SCC.

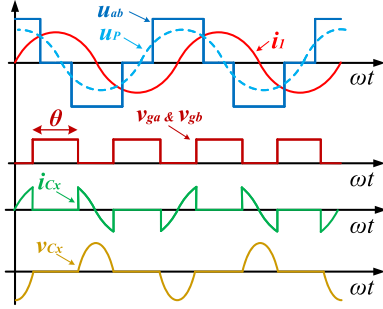


Fig. 6. Typical operating waveforms of the adopted SCC.

shown in Fig. 10, the optimal control variables are calculated offline and stored as a look-up table in the microcontrollers. Based on the duty cycle D_S and the look-up table, the corresponding optimal control variables D_P , δ , and θ are obtained. Finally, with the obtained control outputs, the corresponding driving signals for the inverter, the rectifier, as well as the SCC, are generated by the pulse generators. Notably, the proposed approach uses only one PI controller, eliminating coupling issues of multiple controllers. In addition, the proposed method streamlines feedback control by measuring only dc signals. Thanks to the simplified controller design, stability issues are not a significant concern in the proposed approach.

B. Impact of SCC Tuning

To minimize reactive power, a primary-side SCC is implemented to replace the compensation capacitor C_1 , as shown in Fig. 5. Within the adopted SCC, the capacitor C_x is connected in parallel with two reverse-connected power switches (S_a and S_b), while C_y is employed to reduce the voltage stress across C_x . Typical operating waveforms of the SCC are further shown in Fig. 6. By regulating the conduction angle θ , as shown in Fig. 6, the equivalent capacitance of the SCC can be adjusted. According to the analysis in [24], the SCC equivalent capacitance is given by

$$C_{1_eq} = \frac{\pi C_x C_y}{\pi C_x + \pi C_y - \theta C_y - \sin(\theta) C_y}. \quad (11)$$

To investigate the impact of SCC tuning, the capacitor tuning factor ε is introduced and defined as

$$\varepsilon = \frac{\omega L_1 - 1/(\omega C_{1_eq})}{X_1} \quad (12)$$

where $X_1 = \omega L_{f1}$ is the primary characteristic reactance. As evident from (12), by regulating the SCC equivalent capacitance, the capacitor tuning factor ε is adjusted accordingly. For ease of analysis, ε will be utilized to indicate the SCC tuning degree in

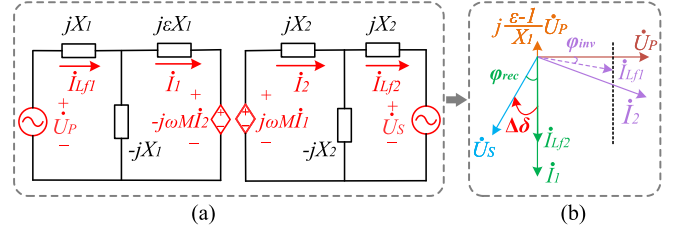


Fig. 7. (a) Simplified FHA model and (b) phase diagrams of voltages and currents for the SCC-based WPT system.

the rest of this article. With the definition of ε and ignoring the loss resistances, the equivalent FHA model of the SCC-based system is simplified in Fig. 7(a), while the corresponding phase diagram of voltages and currents is illustrated in Fig. 7(b). In this model, $X_2 = \omega L_{f2}$ indicates the secondary characteristic reactance. Moreover, applying KVL to this model, the influence of SCC tuning on the system characteristics is analyzed as follows.

1) *Coil Currents*: Based on the FHA method, the expressions for the coil currents \dot{I}_1 and \dot{I}_2 are derived as

$$\dot{I}_1 = -j \frac{\dot{U}_P}{X_1}, \dot{I}_2 = j \frac{\dot{U}_S}{X_2}. \quad (13)$$

Observing (13) reveals that the coil currents \dot{I}_1 and \dot{I}_2 are only determined by the ac voltages \dot{U}_P and \dot{U}_S , remaining unaffected by the SCC tuning.

2) *Inductor Currents*: In addition, the expressions of the inductor currents $\dot{I}_{L_{f1}}$ and $\dot{I}_{L_{f2}}$ are derived as

$$\dot{I}_{L_{f2}} = -j \frac{\omega M}{X_1 X_2} \dot{U}_P \quad (14)$$

$$\dot{I}_{L_{f1}} = j \frac{\varepsilon - 1}{X_1} \dot{U}_P + j \frac{\omega M}{X_1 X_2} \dot{U}_S. \quad (15)$$

As illustrated in (14), the SCC tuning does not affect the secondary inductor current $\dot{I}_{L_{f2}}$. However, further observation of (15) indicates that both the amplitude and the phase angle of the primary inductor current $\dot{I}_{L_{f1}}$ can be adjusted by the SCC tuning. As shown in Fig. 7(b), by incorporating the SCC tuning, a new control variable ε is introduced to facilitate the inverter ZVS by dynamically regulating $\dot{I}_{L_{f1}}$. Furthermore, through simultaneously tuning the SCC and the compensation angle $\Delta\delta$, it is feasible to achieve the inverter and rectifier ZVS with minimal reactive power on both the primary and secondary sides. Details of how to tune ε and $\Delta\delta$ for achieving dual-side optimal ZVS will be elaborated in Section III-C.

3) *Output Power*: To investigate the impact of SCC tuning on the power delivery, the output power expression of the SCC-based system is derived by

$$P_{out} = \text{Re}\{\dot{U}_S \dot{I}_{L_{f2}}^*\} = \frac{M}{\omega L_{f1} L_{f2}} |\dot{U}_P| |\dot{U}_S| \sin\left(\frac{\pi}{2} + \Delta\delta\right). \quad (16)$$

As shown in (16), the SCC tuning does not influence the system output power.

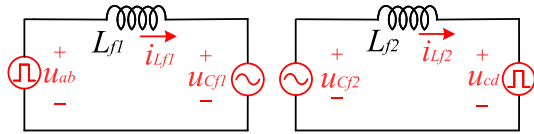


Fig. 8. Harmonic-considered equivalent circuit model for ZVS analysis.

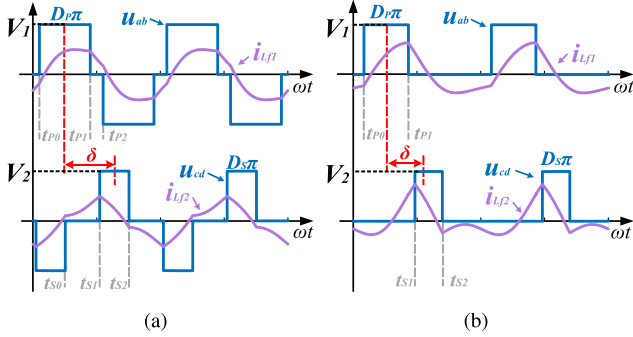


Fig. 9. Typical operating waveforms of the hybrid modes: (a) the FB-FB mode and (b) the HB-HB mode.

C. ZVS Analysis Under Hybrid Modes

Although it is feasible to simultaneously regulate the SCC tuning factor ε and the compensation angle $\Delta\delta$ to achieve dual-side ZVS, the values of ε and $\Delta\delta$ need to be optimized for minimal reactive power. Moreover, as hybrid modulation is considered to improve efficiency under light loads, it is also essential to analyze ZVS conditions in hybrid modes. Therefore, a detailed description of how to optimize ε and $\Delta\delta$ under the hybrid modes is provided in this section.

As the high-order harmonics in $i_{L_{f1}}$ and $i_{L_{f2}}$ are notable, it is important to establish a harmonic-considered model to calculate $i_{L_{f1}}$ and $i_{L_{f2}}$ for ZVS analysis. Due to the filtering effect of L_{f1} , C_{f1} , L_{f2} , and C_{f2} , the voltages across C_{f1} and C_{f2} , denoted as $u_{C_{f1}}$ and $u_{C_{f2}}$, contain little high-order harmonics. Hence, the high-order harmonics in $u_{C_{f1}}$ and $u_{C_{f2}}$ can be ignored [11]. Furthermore, ignoring the loss resistances, the harmonic-considered equivalent circuit model for ZVS analysis is presented in Fig. 8. In this model, $u_{C_{f1}}$ and $u_{C_{f2}}$ are still approximated as sinusoidal waveforms, while the high-order harmonics in u_{ab} and u_{cd} are considered. Based on this model, ZVS analysis under the hybrid modes is presented as follows. In the following analysis, it is important to clarify that the FB-HB mode represents the inverter operating in FB mode while the rectifier operates in HB mode.

1) *FB-FB Mode*: Typical operating waveforms of the FB-FB mode are shown in Fig. 9(a). For the FB-FB mode, the time-domain expressions of $u_{C_{f1}}(t)$ and $u_{C_{f2}}(t)$ are

$$u_{C_{f1}}(t) = \frac{4\varepsilon V_1}{\pi} \sin\left(\frac{D_P\pi}{2}\right) \sin(\omega t) - \frac{4MV_2}{\pi L_{f2}} \sin\left(\frac{D_S\pi}{2}\right) \times \cos(\omega t - \Delta\delta) \quad (17)$$

$$u_{C_{f2}}(t) = \frac{4MV_1}{\pi L_{f1}} \sin\left(\frac{D_P\pi}{2}\right) \sin(\omega t) - \frac{4V_2}{\pi} \sin\left(\frac{D_S\pi}{2}\right) \times \cos(\omega t - \Delta\delta). \quad (18)$$

Moreover, applying KVL to the model, as shown in Fig. 8, the following differential equations are obtained as

$$u_{ab} - u_{C_{f1}} = L_{f1} \frac{di_{L_{f1}}}{dt}, u_{C_{f2}} - u_{cd} = L_{f2} \frac{di_{L_{f2}}}{dt}. \quad (19)$$

By solving the above equations, expressions of $i_{L_{f1}}(t)$ and $i_{L_{f2}}(t)$ can be derived.

Taking $i_{L_{f1}}(t)$ as an example, observing Fig. 9(a) indicates that the inverter output voltage u_{ab} remains at V_1 when $t_{P0} < t < t_{P1}$. Within this time period, the expression of $i_{L_{f1}}(t)$ is

$$i_{L_{f1}}(t) = i_{L_{f1}}(t_{P0}) + \frac{1}{L_{f1}} \int_{t_{P0}}^t [V_1 - u_{C_{f1}}(\tau)] d\tau. \quad (20)$$

When $t_{P1} < t < t_{P2}$, it is evident that $u_{ab} = 0$, and $i_{L_{f1}}(t)$ is expressed as

$$i_{L_{f1}}(t) = i_{L_{f1}}(t_{P1}) + \frac{1}{L_{f1}} \int_{t_{P1}}^t [-u_{C_{f1}}(\tau)] d\tau. \quad (21)$$

Considering the symmetric characteristic of $i_{L_{f1}}(t)$, it is apparent that $i_{L_{f1}}(t_{P0}) = -i_{L_{f1}}(t_{P2})$. Consequently, $i_{L_{f1}}(t_{P0})$ is derived as

$$i_{L_{f1}}(t_{P0}) = -\frac{V_1 D_P \pi}{2\omega L_{f1}} + \frac{4\varepsilon V_1}{\pi\omega L_{f1}} \sin^2\left(\frac{D_P\pi}{2}\right) + \frac{4MV_2}{\pi\omega L_{f1} L_{f2}} \sin\left(\frac{D_S\pi}{2}\right) \cos\left(\frac{D_P\pi}{2} + \Delta\delta\right). \quad (22)$$

Similarly, $i_{L_{f2}}(t_{S2})$ is derived as

$$i_{L_{f2}}(t_{S2}) = -\frac{V_2 D_S \pi}{2\omega L_{f2}} + \frac{4V_2}{\pi\omega L_{f2}} \sin^2\left(\frac{D_S\pi}{2}\right) + \frac{4MV_1}{\pi\omega L_{f1} L_{f2}} \sin\left(\frac{D_P\pi}{2}\right) \cos\left(\frac{D_S\pi}{2} + \Delta\delta\right). \quad (23)$$

According to [11], to realize the inverter and rectifier ZVS with minimal reactive power on both the primary and secondary sides, the following constraint should be satisfied:

$$i_{L_{f1}}(t_{P0}) = -I_{ZVS}, i_{L_{f2}}(t_{S2}) = -I_{ZVS}. \quad (24)$$

Apparently, under the asymmetric parameters, only adjusting the compensation angle $\Delta\delta$ is not feasible to simultaneously satisfy these two equations in (24). Therefore, a new control variable, i.e., the SCC tuning factor ε , is introduced to facilitate dual-side optimal ZVS. Substituting (23) into (24) yields the optimal $\Delta\delta_{\text{opt}}$, which is expressed as

$$\Delta\delta_{\text{opt}} = -D_S\pi/2 + \cos^{-1}\{\Lambda^{-1} \times [-2\pi\omega L_{f1} L_{f2} I_{ZVS} + V_2 L_{f1} (D_S\pi^2 - 8\sin^2(D_S\pi/2))]\} \quad (25)$$

where $\Lambda = 8MV_1 \sin(D_P\pi/2)$. Moreover, substituting (22) and (25) into (24) yields the optimal ε_{opt} , which is

$$\varepsilon_{\text{opt}} = \Gamma^{-1} \times [-2\pi\omega L_{f1} L_{f2} I_{ZVS} + V_1 L_{f2} D_P\pi^2 - 8MV_2 \sin(D_S\pi/2) \cos(D_P\pi/2 + \Delta\delta_{\text{opt}})] \quad (26)$$

where $\Gamma = 8V_1 L_{f2} \sin^2(D_P\pi/2)$.

2) *HB–HB Mode*: Fig. 9(b) presents the typical operating waveforms of the HB–HB mode. For the HB–HB mode, the time-domain expression of $u_{ab}(t)$ is given by

$$\begin{aligned} u_{ab}(t) &= \frac{D_P V_1}{2} + \sum_{n=1,2,\dots} \frac{2V_1}{n\pi} \sin\left(\frac{nD_P\pi}{2}\right) \cos\left[n\left(\omega t - \frac{\pi}{2}\right)\right] \\ &= \frac{D_P V_1}{2} + \sum_{n=1,3,\dots} \frac{2V_1}{n\pi} \sin\left(\frac{nD_P\pi}{2}\right) \sin\left(\frac{n\pi}{2}\right) \sin(n\omega t) \\ &\quad + \sum_{n=2,4,\dots} \frac{2V_1}{n\pi} \sin\left(\frac{nD_P\pi}{2}\right) \cos\left(\frac{n\pi}{2}\right) \cos(n\omega t). \end{aligned} \quad (27)$$

Observing (27) reveals that u_{ab} consists of three parts: the dc component, the odd-harmonics, and the even-harmonics. The impact of these three parts on i_{Lf1} is analyzed as follows. First, due to the dc blocking effect of C_{f1} and C_1 , the dc component of u_{ab} has no impact on i_{Lf1} . Second, the odd-harmonics form a symmetrical FB square waveform, with the dc voltage at $V_1/2$ and the duty cycle at D_P . The calculation of $i_{Lf1_odd}(t)$, which is excited by the odd-harmonics of u_{ab} , can follow the previous analysis for the FB–FB mode. The expression of $i_{Lf1_odd}(t_{P0})$ is derived as

$$\begin{aligned} i_{Lf1_odd}(t_{P0}) &= -\frac{V_1 D_P \pi}{4\omega L_{f1}} + \frac{2\varepsilon V_1}{\pi\omega L_{f1}} \sin^2\left(\frac{D_P\pi}{2}\right) \\ &\quad + \frac{2MV_2}{\pi\omega L_{f1}L_{f2}} \sin\left(\frac{D_S\pi}{2}\right) \cos\left(\frac{D_P\pi}{2} + \Delta\delta\right). \end{aligned} \quad (28)$$

Third, regarding the even-harmonics, the time-domain expression of $i_{Lf1_even}(t)$, which represents the current excited by the even-harmonics, is given by

$$i_{Lf1_even}(t) = \sum_{n=2,4,\dots} \frac{2V_1 \sin(n\omega t)}{n^2\pi\omega L_{f1}} \sin\left(\frac{nD_P\pi}{2}\right) \cos\left(\frac{n\pi}{2}\right). \quad (29)$$

Furthermore, $i_{Lf1_even}(t_{P0})$ is calculated as

$$i_{Lf1_even}(t_{P0}) = \sum_{n=2,4,\dots} \frac{-2V_1}{n^2\pi\omega L_{f1}} \sin^2\left(\frac{nD_P\pi}{2}\right). \quad (30)$$

Consequently, $i_{Lf1}(t_{P0})$ in the HB–HB mode is derived as

$$\begin{aligned} i_{Lf1}(t_{P0}) &= -\frac{V_1 D_P \pi}{4\omega L_{f1}} + \frac{2\varepsilon V_1}{\pi\omega L_{f1}} \sin^2\left(\frac{D_P\pi}{2}\right) \\ &\quad + \frac{2MV_2}{\pi\omega L_{f1}L_{f2}} \sin\left(\frac{D_S\pi}{2}\right) \cos\left(\frac{D_P\pi}{2} + \Delta\delta\right) \\ &\quad - \sum_{n=2,4,\dots} \frac{2V_1}{n^2\pi\omega L_{f1}} \sin^2\left(\frac{nD_P\pi}{2}\right). \end{aligned} \quad (31)$$

Similarly, $i_{Lf2}(t_{S2})$ under the HB–HB mode is derived as

$$\begin{aligned} i_{Lf2}(t_{S2}) &= -\frac{V_2 D_S \pi}{4\omega L_{f2}} + \frac{2V_2}{\pi\omega L_{f2}} \sin^2\left(\frac{D_S\pi}{2}\right) \\ &\quad + \frac{2MV_1}{\pi\omega L_{f1}L_{f2}} \sin\left(\frac{D_P\pi}{2}\right) \cos\left(\frac{D_S\pi}{2} + \Delta\delta\right) \end{aligned}$$

$$- \sum_{n=2,4,\dots} \frac{2V_2}{n^2\pi\omega L_{f2}} \sin^2\left(\frac{nD_S\pi}{2}\right). \quad (32)$$

Interestingly, as shown in (31) and (32), the even-harmonics resulted from the HB mode reduce the values of $i_{Lf1}(t_{P0})$ and $i_{Lf2}(t_{S2})$, which facilitates the implementation of ZVS. Moreover, substituting (32) into (24) yields the optimal $\Delta\delta_{opt}$ under the HB–HB mode, which is

$$\begin{aligned} \Delta\delta_{opt} &= -D_S\pi/2 + \cos^{-1}\left\{\Lambda^{-1} \times \left[-4\pi\omega L_{f1}L_{f2}I_{ZVS} \right. \right. \\ &\quad \left. \left. + V_2L_{f1}(D_S\pi^2 - 8\sin^2(D_S\pi/2)) \right. \right. \\ &\quad \left. \left. + \sum_{n=2,4,\dots} \frac{8V_2L_{f1}}{n^2} \sin^2\left(\frac{nD_S\pi}{2}\right)\right]\right\}. \end{aligned} \quad (33)$$

Further substituting (31) and (33) into (24) obtains the optimal ε_{opt} under the HB–HB mode, which is expressed as

$$\begin{aligned} \varepsilon_{opt} &= \Gamma^{-1} \times \left[-4\pi\omega L_{f1}L_{f2}I_{ZVS} + V_1L_{f2}D_P\pi^2 \right. \\ &\quad \left. - 8MV_2 \sin(D_S\pi/2) \cos(D_P\pi/2 + \Delta\delta_{opt}) \right. \\ &\quad \left. + \sum_{n=2,4,\dots} \frac{8V_1L_{f2}}{n^2} \sin^2\left(\frac{nD_P\pi}{2}\right)\right]. \end{aligned} \quad (34)$$

3) *FB–HB and HB–FB Modes*: The optimal $\Delta\delta_{opt}$ and ε_{opt} under the FB–HB and the HB–FB modes can be derived in a similar way. Specifically, the optimal $\Delta\delta_{opt}$ and ε_{opt} under the FB–HB mode are derived as

$$\begin{aligned} \Delta\delta_{opt} &= -D_S\pi/2 + \cos^{-1}\left\{(2\Lambda)^{-1} \times \left[-4\pi\omega L_{f1}L_{f2}I_{ZVS} \right. \right. \\ &\quad \left. \left. + V_2L_{f1}(D_S\pi^2 - 8\sin^2(D_S\pi/2)) \right. \right. \\ &\quad \left. \left. + \sum_{n=2,4,\dots} \frac{8V_2L_{f1}}{n^2} \sin^2\left(\frac{nD_S\pi}{2}\right)\right]\right\} \end{aligned} \quad (35)$$

$$\begin{aligned} \varepsilon_{opt} &= \Gamma^{-1} \times \left[-2\pi\omega L_{f1}L_{f2}I_{ZVS} + V_1L_{f2}D_P\pi^2 \right. \\ &\quad \left. - 4MV_2 \sin(D_S\pi/2) \cos(D_P\pi/2 + \Delta\delta_{opt})\right]. \end{aligned} \quad (36)$$

Moreover, the optimal $\Delta\delta_{opt}$ and ε_{opt} under the HB–FB mode are obtained as

$$\begin{aligned} \Delta\delta_{opt} &= -D_S\pi/2 + \cos^{-1}\left\{(\Lambda/2)^{-1} \times \left[-2\pi\omega L_{f1}L_{f2}I_{ZVS} \right. \right. \\ &\quad \left. \left. + V_2L_{f1}(D_S\pi^2 - 8\sin^2(D_S\pi/2))\right]\right\} \end{aligned} \quad (37)$$

$$\begin{aligned} \varepsilon_{opt} &= \Gamma^{-1} \times \left[-4\pi\omega L_{f1}L_{f2}I_{ZVS} + V_1L_{f2}D_P\pi^2 \right. \\ &\quad \left. - 16MV_2 \sin(D_S\pi/2) \cos(D_P\pi/2 + \Delta\delta_{opt}) \right. \\ &\quad \left. + \sum_{n=2,4,\dots} \frac{8V_1L_{f2}}{n^2} \sin^2\left(\frac{nD_P\pi}{2}\right)\right]. \end{aligned} \quad (38)$$

Based on the above analysis, it is evident that by simultaneously tuning $\Delta\delta$ and ε to $\Delta\delta_{opt}$ and ε_{opt} , both the inverter and rectifier ZVS can be achieved with minimal reactive power.

D. Derivation of Optimal Control Variables

Distinct from the conventional TPS, the proposed method adopts a multivariable control featuring six degrees of freedom, which makes it challenging to derive an explicit expression of the efficiency, especially for the high-order compensation topology. In addition, it is preferable to consider the overall efficiency of the entire system instead of the efficiency of the resonant tank. Therefore, the traditional approach of identifying the maximum efficiency point by solving the derivative of an explicit efficiency expression is discarded, while it is transformed into an optimization problem with a multivariable input.

The objective of the optimization problem is to minimize the overall losses of the whole system. The power losses of the proposed system comprise the losses incurred by the inverter, the resonant circuits, the SCC, and the rectifier. The power losses of the inverter mainly consist of the conduction and switching losses of the MOSFETs. Specifically, the conduction losses of the inverter are

$$P_{\text{inv_con}} = 2R_{\text{ON}}I_{Lf1}^2 \quad (39)$$

where R_{on} is the conduction resistance of the power switches. Moreover, the switching losses of the inverter are

$$P_{\text{inv_sw}} = \zeta [i_{Lf1}(t_{P0}) + i_{Lf1}(t_{P1})] V_1 \left(\frac{E_{\text{OFF}}}{V_R I_R} + \frac{Q_{RR}}{I_{RD}} \right) f_s \quad (40)$$

where $\zeta = 2$ corresponds to the FB mode, whereas $\zeta = 1$ corresponds to the HB mode; E_{off} represents the turn-OFF energy losses of the MOSFET; V_R and I_R denote the reference drain-source voltage and source current of the MOSFET; and Q_{RR} and I_{RD} are the reverse recovery charge and the reference current of the body diode, respectively [18]. Similarly, the conduction and switching losses of the rectifier are

$$P_{\text{rec_con}} = 2R_{\text{ON}}I_{Lf2}^2 \quad (41)$$

$$P_{\text{rec_sw}} = \zeta [i_{Lf2}(t_{S1}) + i_{Lf2}(t_{S2})] V_1 \left(\frac{E_{\text{OFF}}}{V_R I_R} + \frac{Q_{RR}}{I_{RD}} \right) f_s. \quad (42)$$

In addition, the power losses of the resonant circuits are

$$P_{\text{res}} = I_{Lf1}^2 R_{Lf1} + I_{Lf2}^2 R_{Lf2} + I_1^2 R_1 + I_2^2 (R_2 + R_{C2}) + I_{Cf1}^2 R_{Cf1} + I_{Cf2}^2 R_{Cf2} \quad (43)$$

where R_{C2} , R_{Cf1} , and R_{Cf2} are the equivalent series resistances (ESRs) of the compensation capacitors C_2 , C_{f1} , and C_{f2} , respectively. Moreover, the power losses of the adopted SCC are

$$P_{\text{scc}} = 2I_{ab}^2 R_{\text{ON}} + I_{C_x}^2 R_{C_x} + I_1^2 R_{C_y} \quad (44)$$

where R_{C_x} and R_{C_y} are the ESRs of the compensation capacitors C_x and C_y , respectively; I_{ab} is the rms current across the power switches S_a and S_b ; and I_{C_x} is the rms current across C_x . Consequently, the overall loss of the system is obtained by

$$P_l = P_{\text{inv_con}} + P_{\text{inv_sw}} + P_{\text{rec_con}} + P_{\text{rec_sw}} + P_{\text{res}} + P_{\text{scc}}. \quad (45)$$

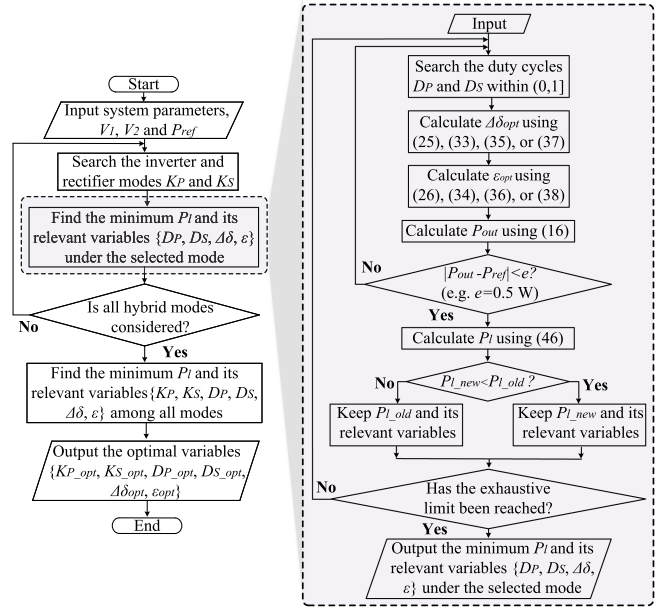


Fig. 10. Flowchart for deriving the optimal variables to minimize the overall power loss of the system.

With given system parameters and dc voltages, P_l can be expressed as

$$P_l = f(D_P, D_S, \Delta\delta, \varepsilon, K_P, K_S). \quad (46)$$

As indicated by (46), P_l is a function determined by six control variables. The optimization objective is to find an optimal set of variables $\{D_{P_opt}, D_{S_opt}, \Delta\delta_{opt}, \varepsilon_{opt}, K_{P_opt}, K_{S_opt}\}$ that minimizes the value of P_l .

The flowchart for deriving the optimal variables is illustrated in Fig. 10, and the specific steps are elaborated as follows. (*Initialization*): First, the system parameters, the dc input, and output voltages V_1 and V_2 , as well as the required output power P_{ref} , are given in the initial stage. (*Mode Selection*): Subsequently, the inverter and rectifier modes K_P and K_S are searched between the FB and HB modes. (*Duty Cycle Selection*): After K_P and K_S are determined, the inverter and rectifier duty cycles D_P and D_S are then searched within the range of (0,1], where the exhaustive method is applied to implement the search of D_P and D_S .

(*Optimal ZVS Implementation*): Based on the selected K_P , K_S , D_P , and D_S , the optimal variables $\Delta\delta_{opt}$ and ε_{opt} are calculated according to the analysis in Section III-B. (*Power Assessment*): After all of the control variables, i.e., D_P , D_S , $\Delta\delta$, ε , K_P , and K_S , are determined, the output power of the system is calculated using (16). If the output power P_{out} is consistent with the required power P_{ref} , the currently selected variables are preserved, and the overall power losses P_l are then calculated using (46).

(*Loss Minimization*): By comparing the power losses P_l obtained from different sets of variables, the optimal set of variables $\{D_{P_opt}, D_{S_opt}, \Delta\delta_{opt}, \varepsilon_{opt}, K_{P_opt}, K_{S_opt}\}$ that minimizes P_l is identified.

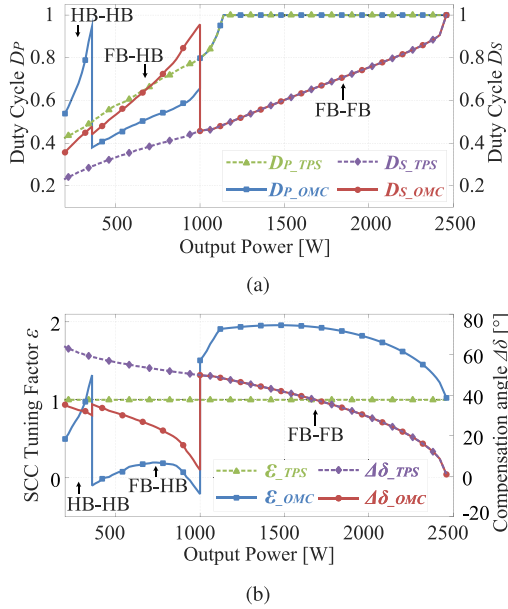


Fig. 11. Derived optimal control variables: (a) the duty cycles D_P and D_S and (b) the compensation phase angle $\Delta\delta$ and the SCC tuning factor ε .

Based on the above approach, the optimal variables are derived using the parameters listed in Table I, as shown in Fig. 11. In addition, the control variables of the existing TPS method are also demonstrated for comparison. As indicated by Fig. 11, the proposed OMC method introduces the HB-HB ($P_{out} \leq 360$ W) and FB-HB (360 W $< P_{out} \leq 1000$ W) modes under light-loads. As illustrated in Fig. 11(b), the introduction of hybrid modes and SCC tuning in the OMC method significantly reduces the value of $\Delta\delta$. The reduced $\Delta\delta$ contributes to decreased reactive power within the resonant circuits, thus achieving improved efficiency under light-load conditions. As the output power approaches full level, both the proposed OMC method and the TPS method operate in the FB-FB mode ($P_{out} > 1000$ W). However, as shown in Fig. 11(b), the SCC tuning is introduced in the OMC method. The incorporation of SCC tuning enables adjustment of both the amplitude and phase angle for the primary inductor current (i_{Lf1}), facilitating optimal ZVS for both the inverter and rectifier. The implementation of dual-side optimal ZVS reduces excessive reactive power caused by asymmetric parameters, thereby further enhancing efficiency under heavy-load conditions.

In practical applications, considering the limited computing power of the microcontrollers, it is preferable to implement the abovementioned optimal control variables using a look-up table. It is noteworthy that the value of SCC conduction angle θ instead of the SCC tuning factor ε should be stored as a look-up table in practical implementation.

E. Design Guidelines for SCC

1) *Capacitance of C_x and C_y* : Based on the optimal variables shown in Fig. 11(b), the maximum and minimum SCC tuning factor is: $\varepsilon_{max} = 1.96$ and $\varepsilon_{min} = -0.21$, respectively. Submitting ε_{max} and ε_{min} into (12) yields the maximum and

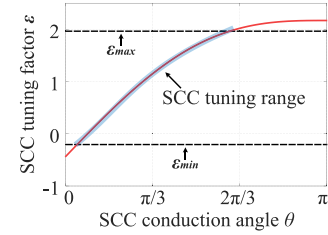


Fig. 12. Relationship between the SCC conduction angle θ and the capacitor tuning factor ε when $C_x = 13.0$ nF and $C_y = 31.7$ nF.

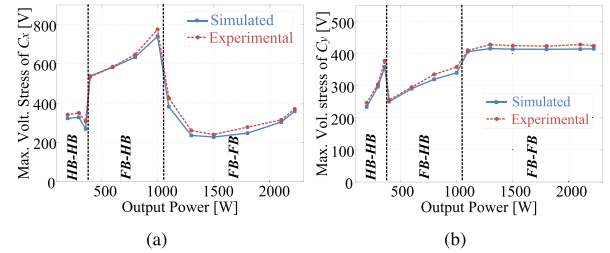


Fig. 13. Maximum voltage stresses of (a) the capacitor C_x and (b) the capacitor C_y under different power levels.

minimum capacitance of C_{1_eq} , i.e., $C_{1_eq_max} = 26.5$ nF and $C_{1_eq_min} = 9.8$ nF, respectively. On the other hand, regarding the tuning range of θ ($0 \leq \theta \leq \pi$), the equivalent SCC capacitance satisfies: $C_x/C_y \leq C_{1_eq} \leq C_y$. To ensure that the SCC is able to obtain the required capacitance, the following relationship should be satisfied: $C_y \geq 26.5$ nF, $C_x/C_y \leq 9.8$ nF. Moreover, as shown in Fig. 12, when θ approaches π , the $\theta - \varepsilon$ curve becomes flat. The flattened curve area significantly reduces the SCC tuning sensitivity. Therefore, to prevent encountering this area, it is important to consider sufficient margins when designing C_x and C_y . Consequently, the capacitance of C_x and C_y are designed as 13.0 and 31.7 nF, respectively.

2) *Voltage stress of SCC*: To illustrate the capacitor voltage stresses of the SCC, Fig. 13 demonstrates the simulation results of the maximum capacitor voltages at different power levels. As the output power varies, the simulated maximum voltage stresses of C_x and C_y reach up to 740 and 415 V, respectively. Moreover, the measured maximum voltage stresses of C_x and C_y in the experiments are also presented in Fig. 13 for comparisons. As depicted in Fig. 13, the experimental results demonstrate good agreement with the simulated results.

Following the above analysis, the selection of SCC MOSFETs can be facilitated. According to the SCC topology, the switches S_a and S_b need to block the voltage of C_x when the switches are turned OFF. Based on the above simulation analysis for SCC voltage stress, the rated blocking voltage of S_a and S_b should exceed 740 V. It is noteworthy that in practical applications, sufficient margins should be considered when selecting MOSFETs. Therefore, in this article, MOSFETs with a rated voltage of 1.2 kV are selected as the SCC switches.

IV. EXPERIMENTAL VERIFICATIONS

A. Hardware Setup

To validate the proposed OMC method, experiments were carried out based on an LCC-LCC compensated WPT prototype,

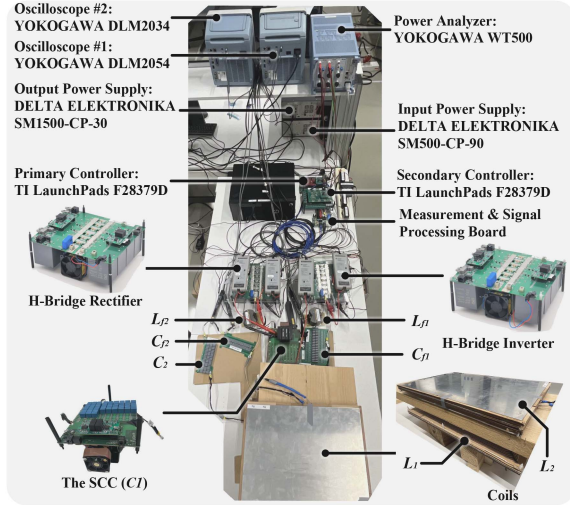


Fig. 14. Experimental prototype.

 TABLE III
 HARDWARE CONFIGURATIONS OF THE INVESTIGATED WPT PROTOTYPE

Configurations	Descriptions
Converter switches	SiC MOSFETS (IMZ120R030M1H)
SCC switches (S_a, S_b)	SiC MOSFETS (G3R20MT12K)
Capacitors (C_{f1}, C_{f2}, C_2)	Film capacitors (KEMET R76)
Capacitors (C_x, C_y)	Film capacitors (TDK B32671L)
Inductor cores (L_{f1}, L_{f2})	Ferrites (TDK PM 74/59, N87)
Coil dimensions (L_1, L_2)	58 cm \times 38 cm
Coil turns (L_1, L_2)	$N_1 = 19, N_2 = 20$
Litz wire (L_1, L_2)	600 strands \times 0.071 mm
Air gap of coils (L_1, L_2)	10 cm

as depicted in Fig. 14. Within this prototype, the asymmetric coil structure is investigated, and the inductors L_{f1} and L_{f2} are designed to obtain the required maximum output power. The capacitors C_2, C_{f1} , and C_{f2} are designed in accordance with the general principles of the LCC-LCC topology, while the capacitor C_1 is replaced by an SCC. The switching frequency is set to the commonly adopted 85 kHz within WPT systems. In addition, a nonunity dc voltage gain is considered, with the dc voltages configured as $V_1 = 300$ V and $V_2 = 500$ V, respectively. Moreover, the proposed control algorithm, as well as the pulse generation for the converters and the SCC, was implemented on the TI LaunchPad F28379D. The synchronization between the primary and secondary sides is achieved by the zero-crossing-detection technique for the secondary coil current. To guarantee ZVS for the inverter and rectifier, the minimum ZVS current of the power switches is designed as 2.0 A. More detailed system parameters and hardware configurations of the investigated prototype are elaborated in Tables I and III, respectively.

B. Operating Waveforms and Efficiency Comparisons

When delivering 300 W power in the proposed OMC method, as illustrated in Fig. 15, the system operates in the HB-HB mode. Moreover, in the proposed method, the SCC tuning factor ε ,

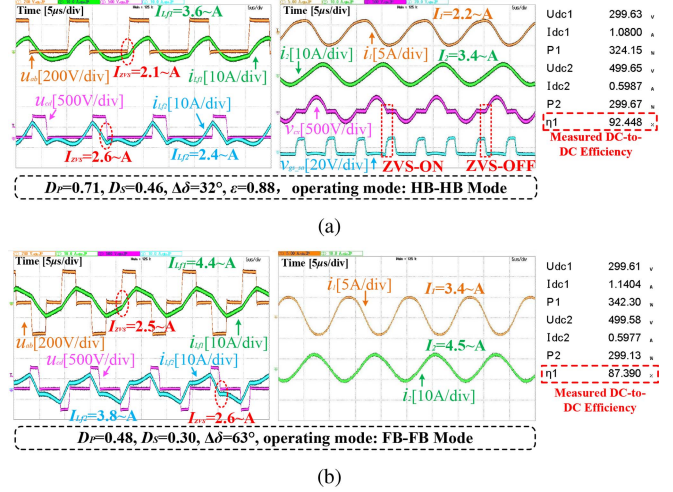


Fig. 15. Measured operating waveforms and DC-to-DC efficiency when delivering 300 W power: (a) the proposed OMC method and (b) the existing TPS method.

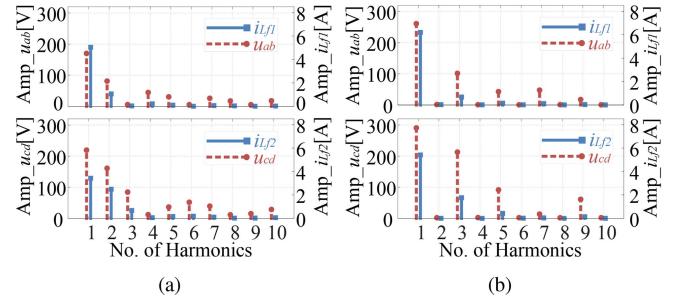


Fig. 16. Harmonic analysis for the experiments shown in Fig. 15: (a) the proposed OMC method and (b) the existing TPS method.

as well as the compensation angle $\Delta\delta$, is adjusted to achieve both the inverter and rectifier ZVS while minimizing the reactive power. Specifically, the SCC tuning factor ε is regulated to 0.88, while the compensation angle $\Delta\delta$ is adjusted to 32° . In addition, as demonstrated in Fig. 15, by incorporating the HB-HB mode, the proposed OMC method notably increases the values of D_P and D_S . The incorporation of HB-HB mode and SCC tuning significantly reduces the compensation angle $\Delta\delta$ from 63° to 32° in the proposed method, consequently lowering reactive power within the resonant circuits. The reduction of reactive power contributes to a notable decrease in the rms values of the inductor and coil currents. In comparison with the TPS method, as demonstrated in Fig. 15, the proposed method reduces I_{Lf1} from 4.4 to 3.6 A, I_{Lf2} from 3.8 to 2.4 A, I_1 from 3.4 to 2.2 A, and I_2 from 4.5 to 3.4 A. The decreased rms currents not only result in reduced power losses within the resonant circuits, but also minimize conduction losses of the converters. Furthermore, operating the converters in the HB mode halves the equivalent switching times of the power switches, which also significantly reduces the switching losses of the converters. Consequently, as shown in Fig. 15, the proposed method improves the dc-to-dc efficiency from 87.4% to 92.4%, achieving an efficiency improvement of 5.0%. Fig. 16 further demonstrates the harmonics analysis for

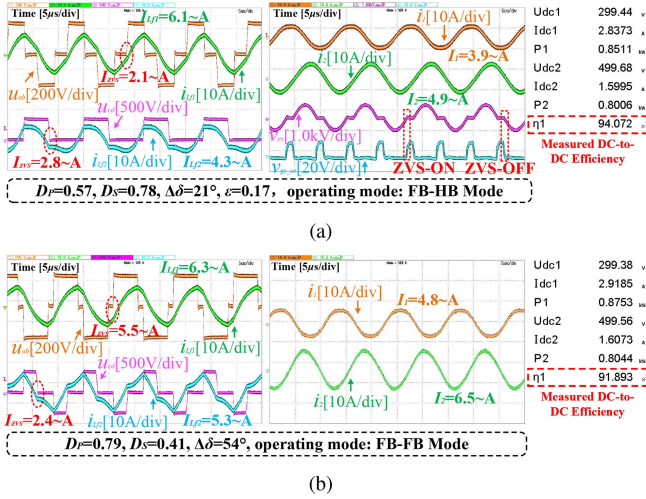


Fig. 17. Measured operating waveforms and DC-to-DC efficiency when delivering 800 W power: (a) the proposed OMC method and (b) the existing TPS method.

the experiments, as shown in Fig. 15. The introduction of the HB–HB mode, as shown in Fig. 16, results in even-harmonics in the ac voltages u_{ab} and u_{cd} , consequently leading to even-harmonics in the inductor currents i_{Lf1} and i_{Lf2} . Although notable harmonics existed within i_{Lf1} and i_{Lf2} , both the inverter and rectifier ZVS were achieved in the proposed method. As illustrated in Fig. 15(a), by simultaneously adjusting ε and $\Delta\delta$, the minimum ZVS currents for the inverter and rectifier were 2.1 and 2.6 A, respectively.

Fig. 17 further presents the experimental results of the proposed method and the TPS method when delivering 800 W. When applying the proposed OMC method to deliver 800 W power, the system works in the FB–HB mode. As demonstrated in Fig. 17(a), the proposed OMC method adjusts the SCC tuning factor ε to 0.17 to enable the inverter ZVS. Moreover, the compensation angle $\Delta\delta$ is reduced from 54° to 21° in the proposed OMC method. The introduction of FB–HB mode and SCC tuning reduces I_{Lf1} from 6.3 to 6.1 A, I_{Lf2} from 5.3 to 4.3 A, I_1 from 4.8 to 3.9 A, and I_2 from 6.5 to 4.9 A. More importantly, by adjusting the SCC, the proposed method reduces the minimum inverter ZVS current from 5.5 to 2.1 A, resulting in a decrease in inverter turn-OFF losses. When delivering 800 W, the proposed method enhances the efficiency from 91.9% to 94.1%, leading to an efficiency improvement of 2.2%.

When delivering 1.5 kW power in the proposed method, as shown in Fig. 18, both the proposed OMC method and the TPS method operate in the FB–FB mode. In both methods, the duty cycles D_P and D_S , as well as the compensation angle $\Delta\delta$, are similar. However, in the proposed OMC method, the SCC tuning factor ε is regulated to 1.95 to facilitate the optimal inverter ZVS. As illustrated in Fig. 18, the proposed method dramatically reduces the minimum ZVS current of the inverter from 10.8 to 2.8 A, leading to a substantial reduction in the inverter turn-OFF losses. Moreover, I_{Lf1} is also decreased from 8.9 to 6.1 A, which lowers the inverter conduction losses and the primary inductor

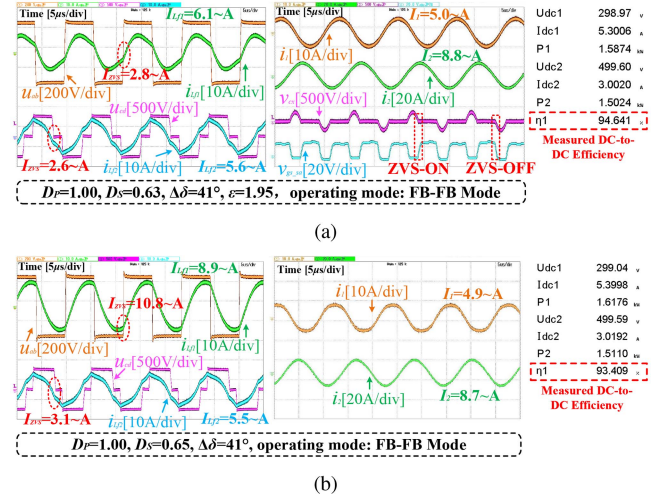


Fig. 18. Measured operating waveforms and DC-to-DC efficiency when delivering 1.5 kW power: (a) the proposed OMC method, (b) the existing TPS method.

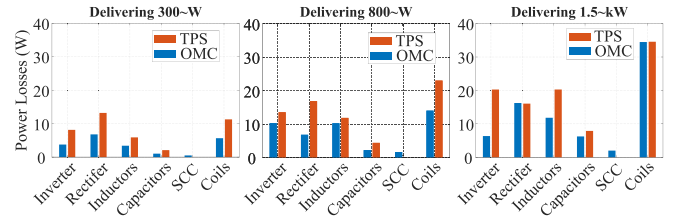


Fig. 19. Calculated power loss distributions for the experiments presented in Figs. 15, 17, and 18.

losses. Compared with the TPS method, the proposed method achieves an efficiency improvement of 1.2%, with the efficiency improved from 93.4% to 94.6%.

Fig. 19 demonstrates the calculated power loss distributions for the above experiments. As illustrated in Fig. 19, owing to the introduction of hybrid modulation and SCC tuning, the losses in the converters, inductors, capacitors, and coils are all reduced when delivering 300 and 800 W power in the proposed method. Moreover, when delivering 1.5 kW power, the incorporation of SCC reduces the primary inductor current and the inverter turn-OFF current, contributing to a significant reduction in the inverter and inductor losses. It is noteworthy that the implementation of ZVS turn-ON and turn-OFF for the SCC (as shown in Figs. 15, 17, and 18) effectively minimizes the SCC switching losses, and extra losses caused by the SCC are insignificant.

Furthermore, Fig. 20 demonstrates the measured dc-to-dc efficiency of the proposed OMC method with the TPS method at different output power levels. As illustrated in Fig. 20, the introduction of hybrid modulation and SCC tuning significantly enhances the efficiency under light-load conditions, resulting in a maximum efficiency improvement of up to 6.3%. The maximum efficiency improvement is observed at 200 W, where the efficiency is improved from 84.3% to 90.6%. In addition to the enhanced efficiency under light-load conditions, the proposed approach further improves efficiency as the output power

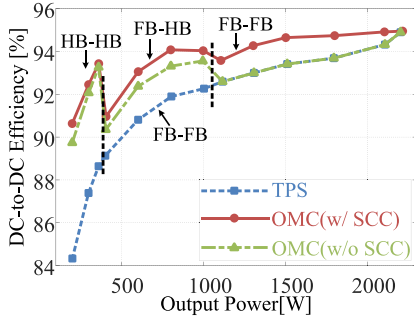


Fig. 20. Measured DC-to-DC efficiency of the proposed OMC method and the TPS method at different output power levels.

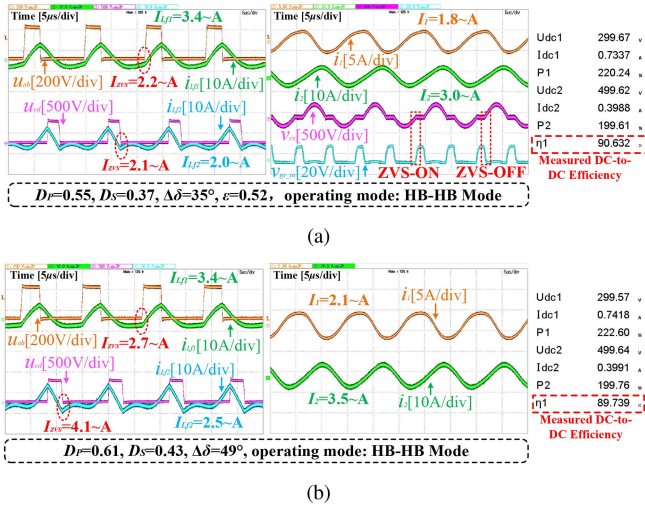
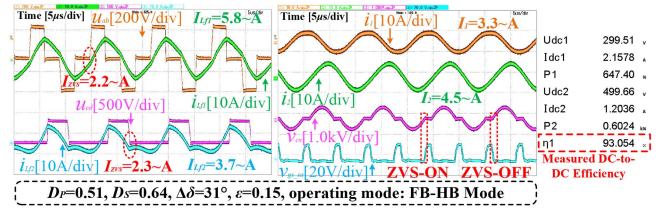


Fig. 21. Measured operating waveforms and DC-to-DC efficiency when delivering 200 W power in the proposed OMC method: (a) with SCC and (b) without SCC.

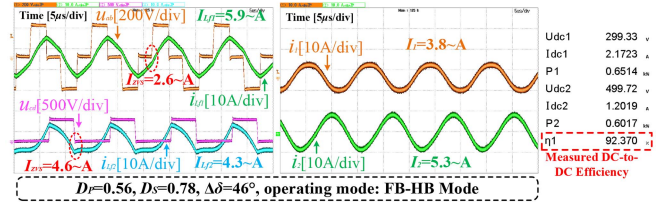
approaches the full level through the implementation of SCC tuning. Consequently, the proposed OMC method enables full-range efficiency optimization, with the efficiency consistently exceeding 90% in the power range of 0.2–2.2 kW.

To demonstrate the benefits of SCC tuning, Fig. 21 presents the experimental results when delivering 200 W power in the HB–HB mode, comparing cases with and without SCC. As shown in Fig. 21(b), only adjusting the compensation angle $\Delta\delta$ fails to achieve dual-side optimal ZVS. To guarantee dual-side ZVS without SCC, $\Delta\delta$ is adjusted to 49° , and the minimum rectifier ZVS current reaches 4.1 A. Conversely, introducing SCC enables both the inverter and rectifier to achieve ZVS with a minimized ZVS current. Furthermore, SCC tuning reduces $\Delta\delta$ from 49° to 35° , resulting in diminished reactive power within the resonant circuits. As demonstrated in Fig. 21, SCC tuning decreases $I_{L,f2}$ from 2.5 to 2.0 A, I_1 from 2.1 to 1.8 A, and I_2 from 3.5 to 3.0 A, achieving an efficiency improvement of 0.9%.

In addition, Fig. 22 compares experimental results for 600 W power delivery in the FB–HB mode with and without SCC. As shown in Fig. 22, introducing SCC lowers the minimum rectifier ZVS current from 4.6 to 2.3 A and decreases $\Delta\delta$ from 46° to 31° . Moreover, it reduces $I_{L,f2}$ from 4.3 to 3.7 A, I_1 from 3.8 to 3.3 A, and I_2 from 5.3 to 4.5 A, leading to an efficiency enhancement of 0.7%.



(a)



(b)

Fig. 22. Measured operating waveforms and DC-to-DC efficiency when delivering 600 W power in the proposed OMC method: (a) with SCC and (b) without SCC.

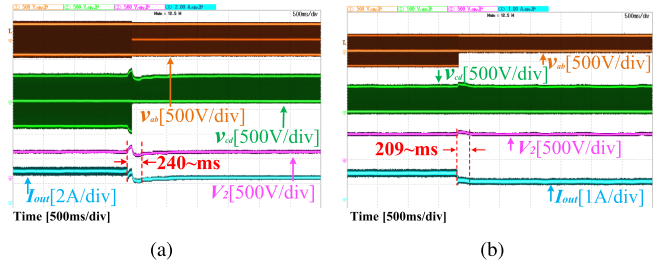


Fig. 23. Dynamic performance of the proposed OMC method: (a) when the DC load is changed from 200 to 250 Ω , with the output power decreased from 1.25 to 1 kW and (b) when the DC load is changed from 500 to 750 Ω , with the output power decreased from 500 to 333.3 W.

The dc-to-dc efficiency with and without SCC tuning under different power levels is also compared in Fig. 20. As demonstrated in Fig. 20, the introduction of SCC improves the efficiency across the entire power range, encompassing HB–HB, FB–HB, and FB–FB modes.

C. Dynamic Performance

To assess the dynamic performance of the proposed OMC method, the experimental prototype was tested under transient load changes. A measurement and signal processing board was designed to monitor the dc output voltage and current in real time. In addition, a PI controller was implemented in the TI launchpads to achieve voltage tracking under load changes.

The dynamic experimental results are demonstrated in Fig. 23. As shown in Fig. 23(a), when the dc load suddenly changes from 200 to 250 Ω , the operating mode of the system shifts from the FB–FB mode to the FB–HB mode. The dc output voltage is restored to 500 V within 240 ms, with the output power decreased from 1.25 to 1.0 kW. As the output power further decreases, the system operating mode switches from the FB–HB mode to the HB–HB mode, as demonstrated in Fig. 23(b). Experiments reveal that when the dc load is abruptly changed from 500 to 750 Ω , the proposed method effectively

TABLE IV
COMPARISONS WITH OTHER EXISTING CONTROL METHODS FOR WIDE OUTPUT REGULATION AND EFFICIENCY OPTIMIZATION

Reference	Compensation	Control scheme	Control variables	Dynamic time	Output power	DC-to-DC efficiency
[10]	SS	Dual-side control	DPS	< 30 ms	0.1–1.0 kW	80%–93%
[11]	<i>LCC–LCC</i>	Dual-side control	TPS	N/A	0.2–1.0 kW	90%–94.83%
[25]	SS	Primary-side control	Inverter PSM ¹ and variable inductor	< 280 ms	57–170 W	77%–92%
[18]	SS	Dual-side control	TPS and hybrid modulation	< 140 ms	0.3–1.8 kW	92.49%–94.29%
[19]	SS	Dual-side control	TPS and hybrid modulation	< 190 ms	1.0–10 kW	93.5%–96.1%
[20]	<i>LCC–LCC</i>	Dual-side control	TPS and SCC	10 ms	0.2–1.6 kW	88.2%–92.3%
This article	<i>LCC–LCC</i>	Dual-side control	TPS, hybrid modulation, and SCC	< 240 ms	0.2–2.2 kW	90.6%–94.9%

¹ PSM indicates phase shift modulation.

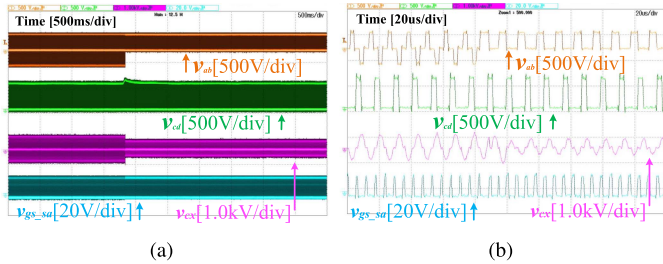


Fig. 24. (a) Dynamic performance of SCC and (b) enlarged view of Fig. 24(a) when the DC load is altered from 500 to 750 Ω .

restores the output voltage to the reference value within 209 ms, with the output power decreased from 500 to 333.3 W. Moreover, Fig. 24 presents the dynamic performance of the SCC when the dc load is altered from 500 to 750 Ω . As illustrated in Fig. 24, by adjusting the SCC conduction angle, the proposed method achieves dynamic SCC tuning under load changes.

D. Comparisons With Existing Methods

Table IV compares the proposed OMC approach with other existing methods. As given in Table IV, [25] incorporated a variable inductor to achieve wide ZVS for the SS compensation. However, Li et al. [25] solely investigated the primary-side control, which is limited in control flexibility and output tuning range. Conversely, the dual-side control provides greater control flexibility and enhances the power regulation range. Nevertheless, the existing DPS control results in hard switching under load variations [10], whereas current TPS methods lead to significant reactive power [11].

Although the authors in [18] and [19] integrated hybrid modulation into the TPS control to improve light-load efficiency, their focus was on SS compensation. To the best of the authors' knowledge, the integration of dual-side hybrid modulation into the TPS method specifically for the *LCC–LCC* topology has not yet been reported. Distinct from the SS topology, where the harmonics of the coil currents can be ignored, hybrid modulation introduces noticeable harmonics into the inductor currents within the *LCC–LCC* topology. With harmonics considered, the proposed method investigates optimal ZVS conditions for all hybrid modes in the *LCC–LCC* topology, enabling ZVS for both the inverter and rectifier while minimizing reactive power.

In addition, we investigated the TPS control for the asymmetric *LCC–LCC* topology. Although existing TPS strategies for *LCC–LCC* compensation primarily concentrate on symmetrical topologies [11], [20], the asymmetric structure is also frequently employed [22], [23]. To this end, we extended the existing analysis to the asymmetric *LCC–LCC* network and presented the limitations of existing TPS methods. Furthermore, we proposed an OMC method by introducing dual-side hybrid modulation and SCC tuning. Although the work in [20] also incorporates the SCC tuning, it does not consider dual-side hybrid modulation and fails to effectively improve the light-load efficiency. Integrating dual-side hybrid modulation and SCC tuning forms a multivariable control featuring six degrees of freedom. Based on the power loss analysis, this article establishes a multivariable optimization problem. By solving this problem, all optimal control variables are derived to minimize the overall loss of the system.

Moreover, Table IV demonstrates comparisons of the power tuning range, dc-to-dc efficiency, and dynamic time. As given in Table IV, the proposed method achieves a dc-to-dc efficiency range of 90.6%–94.9% within 9.1%–100% of rated power. When compared with other listed methods that also utilize the *LCC–LCC* topology, the proposed method achieves higher efficiency across a wider output power regulation range. Regarding dynamic time, the proposed approach exhibits a performance comparable with that of existing methods. Similar to other literature, the proposed method achieves dynamic time at the millisecond (ms) level, which is fast enough for battery charging. Notably, the proposed method aims at wide-range power regulation and efficiency optimization for steady-state operation, whereas reducing dynamic time is not the main focus. In addition, as the dynamic time is affected by system parameters, experimental configurations, and hardware circuits, it is difficult to make a fair comparison of dynamic time across various experimental platforms in different literature.

It is noteworthy that although the SCC leads to extra losses, these losses are not significant due to the low ON-resistance characteristics of MOSFETs and the implementation of zero-voltage turn-ON and turn-OFF for SCC switches. Moreover, although extra switches are required, introducing SCC notably enhances overall system efficiency. This improved efficiency not only conserves more energy but also alleviates the thermal stress of the converters and resonant circuits. Therefore, for applications demanding high energy efficiency, the proposed method is beneficial.

V. CONCLUSION

To facilitate wide output tuning while improving efficiency for the WPT systems, this article proposes an OMC strategy by incorporating SCC tuning and hybrid modulation into the TPS method. Through simultaneously adjusting the converter phase-shift angles and the SCC conduction angle, the proposed approach achieves inverter and rectifier ZVS with minimized reactive power on both the primary and secondary sides. Moreover, the integration of hybrid modulation reduces reactive power under light-load conditions. The reduction in reactive power leads to decreased rms currents, as well as reduced turn-OFF currents, consequently minimizing power losses within the system. Experimental results confirm that the proposed method effectively achieves wide output regulation and full-range efficiency optimization for an LCC-LCC compensated WPT prototype.

REFERENCES

- [1] W. Liu, K. Chau, X. Tian, H. Wang, and Z. Hua, "Smart wireless power transfer—opportunities and challenges," *Renewable Sustain. Energy Rev.*, vol. 180, 2023, Art. no. 113298.
- [2] S. Roy, A. W. Azad, S. Baidya, M. K. Alam, and F. Khan, "Powering solutions for biomedical sensors and implants inside the human body: A comprehensive review on energy harvesting units, energy storage, and wireless power transfer techniques," *IEEE Trans. Power Electron.*, vol. 37, no. 10, pp. 12237–12263, Oct. 2022.
- [3] L. Yang et al., "Undersea wireless power and data transfer system with shared channel powered by marine renewable energy system," *IEEE Trans. Emerg. Sel. Topics Circuits Syst.*, vol. 12, no. 1, pp. 242–250, Mar. 2022.
- [4] M. Amjad, M. Farooq-i Azam, Q. Ni, M. Dong, and E. A. Ansari, "Wireless charging systems for electric vehicles," *Renewable Sustain. Energy Rev.*, vol. 167, 2022, Art. no. 112730.
- [5] Z. Huang, S.-C. Wong, and K. T. Chi, "Control design for optimizing efficiency in inductive power transfer systems," *IEEE Trans. Power Electron.*, vol. 33, no. 5, pp. 4523–4534, May 2018.
- [6] G. Yu, J. Dong, T. B. Soeiro, G. Zhu, Y. Yao, and P. Bauer, "Three-mode variable-frequency ZVS modulation for four-switch buck boost converters with ultra-high efficiency," *IEEE Trans. Power Electron.*, vol. 38, no. 4, pp. 4805–4819, Apr. 2022.
- [7] M. Gheisarnejad, H. Farsizadeh, M.-R. Tavana, and M. H. Khooban, "A novel deep learning controller for DC-DC buck-boost converters in wireless power transfer feeding CPLs," *IEEE Trans. Ind. Electron.*, vol. 68, no. 7, pp. 6379–6384, Jul. 2021.
- [8] Z. Hua, K. Chau, W. Han, W. Liu, and T. W. Ching, "Output-controllable efficiency-optimized wireless power transfer using hybrid modulation," *IEEE Trans. Ind. Electron.*, vol. 69, no. 5, pp. 4627–4636, May 2021.
- [9] R. Mai, Y. Liu, Y. Li, P. Yue, G. Cao, and Z. He, "An active-rectifier-based maximum efficiency tracking method using an additional measurement coil for wireless power transfer," *IEEE Trans. Power Electron.*, vol. 33, no. 1, pp. 716–728, Jan. 2018.
- [10] Y. Li, J. Hu, F. Chen, Z. Li, Z. He, and R. Mai, "Dual-phase-shift control scheme with current-stress and efficiency optimization for wireless power transfer systems," *IEEE Trans. Circuits Syst. I: Reg. Papers*, vol. 65, no. 9, pp. 3110–3121, Sep. 2018.
- [11] X. Zhang et al., "A control strategy for efficiency optimization and wide ZVS operation range in bidirectional inductive power transfer system," *IEEE Trans. Ind. Electron.*, vol. 66, no. 8, pp. 5958–5969, Aug. 2018.
- [12] V. Yenil and S. Cetin, "An improved pulse density modulation control for secondary side controlled wireless power transfer system using LCC-S compensation," *IEEE Trans. Ind. Electron.*, vol. 69, no. 12, pp. 12762–12772, Dec. 2022.
- [13] W. Zhong and S. Hui, "Maximum energy efficiency operation of series-series resonant wireless power transfer systems using on-off keying modulation," *IEEE Trans. Power Electron.*, vol. 33, no. 4, pp. 3595–3603, Apr. 2017.
- [14] A. Mostafa et al., "Output power regulation of a series-series inductive power transfer system based on hybrid voltage and frequency tuning method for electric vehicle charging," *IEEE Trans. Ind. Electron.*, vol. 69, no. 10, pp. 9927–9937, Oct. 2022.
- [15] H. Hu, T. Cai, S. Duan, X. Zhang, J. Niu, and H. Feng, "An optimal variable frequency phase shift control strategy for ZVS operation within wide power range in IPT systems," *IEEE Trans. Power Electron.*, vol. 35, no. 5, pp. 5517–5530, May 2020.
- [16] G. Zhu, J. Dong, F. Grazian, and P. Bauer, "A parameter recognition based impedance tuning method for SS-compensated wireless power transfer systems," *IEEE Trans. Power Electron.*, vol. 38, no. 11, pp. 13298–13314, Nov. 2023.
- [17] G. Zhu, J. Dong, and P. Bauer, "A dynamic frequency sweeping based parameter estimation method for wireless power transfer," in *Proc. IEEE 49th Annu. Conf. Ind. Electron. Soc.*, 2023, pp. 1–6.
- [18] Y. Li, W. Sun, X. Zhu, and J. Hu, "A hybrid modulation control for wireless power transfer systems to improve efficiency under light-load conditions," *IEEE Trans. Ind. Electron.*, vol. 69, no. 7, pp. 6870–6880, Jul. 2021.
- [19] G. Zhu, J. Dong, W. Shi, T. B. Soeiro, J. Xu, and P. Bauer, "A mode-switching-based phase shift control for optimized efficiency and wide ZVS operations in wireless power transfer systems," *IEEE Trans. Power Electron.*, vol. 38, no. 4, pp. 5561–5575, Apr. 2023.
- [20] N. Fu, J. Deng, Z. Wang, and D. Chen, "An LCC-LCC compensated WPT system with switch-controlled capacitor for improving efficiency at wide output voltages," *IEEE Trans. Power Electron.*, vol. 38, no. 7, pp. 9183–9194, Jul. 2023.
- [21] S. Li, W. Li, J. Deng, T. D. Nguyen, and C. C. Mi, "A double-sided LCC compensation network and its tuning method for wireless power transfer," *IEEE Trans. Veh. Technol.*, vol. 64, no. 6, pp. 2261–2273, Jun. 2014.
- [22] W. Shi et al., "Design of a highly efficient 20-kW inductive power transfer system with improved misalignment performance," *IEEE Trans. Transport. Electrification*, vol. 8, no. 2, pp. 2384–2399, Jun. 2022.
- [23] S. Ann and B. K. Lee, "Analysis of impedance tuning control and synchronous switching technique for a semibridgeless active rectifier in inductive power transfer systems for electric vehicles," *IEEE Trans. Power Electron.*, vol. 36, no. 8, pp. 8786–8798, Aug. 2021.
- [24] F. Grazian, T. B. Soeiro, and P. Bauer, "Inductive power transfer based on variable compensation capacitance to achieve an EV charging profile with constant optimum load," *IEEE Trans. Emerg. Sel. Topics Power Electron.*, vol. 11, no. 1, pp. 1230–1244, Feb. 2023.
- [25] Y. Li et al., "Extension of ZVS region of series-series WPT systems by an auxiliary variable inductor for improving efficiency," *IEEE Trans. Power Electron.*, vol. 36, no. 7, pp. 7513–7525, Jul. 2021.



Gangwei Zhu (Student Member, IEEE) was born in Hunan, China, in 1997. He received the B.S. degree in electrical engineering from Central South University, Changsha, China, in 2018, and the M.S. degree in electrical engineering from Shanghai Jiao Tong University, Shanghai, China, in 2021. He is currently working toward the Ph.D. degree in electrical engineering with Delft University of Technology, Delft, The Netherlands.

His research interests include design, modeling, and control for power electronics and wireless power

transfer.



Jianning Dong (Senior Member, IEEE) received the B.S. and Ph.D. degrees in electrical engineering from Southeast University, Nanjing, China, in 2010 and 2015, respectively.

He was a Postdoctoral Researcher with McMaster Automotive Resource Centre, McMaster University, Hamilton, ON, Canada. Since 2016, he has been an Assistant Professor with DC System, Energy Conversion and Storage Group, Delft University of Technology, Delft, The Netherlands. His research interests include electromechanical energy conversion and contactless power transfer.



Guangyao Yu (Student Member, IEEE) was born in Haiyan, Zhejiang, China. He received the bachelor's degree in electrical engineering and automation from Zhejiang University, Hangzhou, China, in 2015, and the master's degree (with cum laude) in electrical engineering in 2020 from the Delft University of Technology, Delft, The Netherlands, where he is currently working toward the Ph.D. degree in electrical engineering with Delft University of Technology, Delft, The Netherlands.

From 2016 to 2018, he was with Solax Power Company, Ltd., Hangzhou, China, where he was an Electrical Engineer. His research interests include modulation study of power electronic converters, PCB design, and wireless power transfer.



Wenli Shi (Student Member, IEEE) received the Ph.D. degree in electric engineering from the Delft University of Technology (TU Delft), Delft, The Netherlands, in 2023.

From 2022 to 2023, he was a Postdoctoral Researcher with DC System, Energy Conversion and Storage, TU Delft, where since May 2023, he has been an Assistant Professor conducting research into transportation electrification. His research interests include wireless power transfer for electric vehicles, electromagnetic actuation for high precision applications, and protection of dc microgrid for electric aircraft.



Calvin Riekerk (Student Member, IEEE) received the B.S. and M.S. degrees in electrical engineering in 2018 and 2020, respectively, from the Delft University of Technology, Delft, The Netherlands, where he is currently working toward the Ph.D. degree in electrical engineering with Delft University of Technology, Delft, The Netherlands.

His research focuses on wireless power transfer.



Pavol Bauer (Senior Member, IEEE) received the master's degree in electrical engineering from the Technical University of Kosice, Kosice, Slovakia, in 1985, and the Ph.D. degree in power electronics from the Delft University of Technology, Delft, The Netherlands, in 1995.

From 2002 to 2003, he was with KEMA (DNV GL), Arnhem, The Netherlands, on different projects related to power electronics applications in power systems. He is currently a Full Professor with the Department of Electrical Sustainable Energy, Delft University of Technology, and the Head of DC Systems, Energy Conversion, and Storage Group. He is also a Professor with the Brno University of Technology, Brno, Czech Republic, and an Honorary Professor with the Politehnica University Timisoara, Timisoara, Romania. He has authored or coauthored more than 120 journal articles and 500 conference papers in his field. He is an author or coauthor of eight books, holds seven international patents, and organized several tutorials at international conferences. He has worked on many projects for the industry concerning wind and wave energy, power electronic applications for power systems, such as Smarttrafo, HVdc systems, projects for smart cities, such as photovoltaic (PV) charging of electric vehicles, PV and storage integration, contactless charging, and he participated in several Leonardo da Vinci and H2020, and Electric Mobility Europe EU projects as a Project Partner (ELINA, INETELE, E-Pragmatic, Micact, Trolley 2.0, OSCD, P2P, and Progressus) and a Coordinator (PEMCWebLab.com-Edipe, SustEner, Eranet DCMICRO).

Dr. Bauer is the Former Chairman of Benelux IEEE Joint Industry Applications Society, Power Electronics and Power Engineering Society Chapter, the Chairman of the Power Electronics and Motion Control Council, a Member of the Executive Committee of European Power Electronics Association, and also a Member of the International Steering Committee at numerous conferences.